

β -Hydrogen Elimination Mechanism in the Absence of Low-Lying Acceptor Orbitals in $\text{EH}_2(t\text{-C}_4\text{H}_9)$ ($\text{E} = \text{N-Bi}$)

Andreas Stegmüller and Ralf Tonner*

Fachbereich Chemie and Material Sciences Center, Philipps-Universität Marburg, Hans-Meerwein-Straße, 35032 Marburg, Germany

S Supporting Information

ABSTRACT: The β -hydrogen elimination reactions of group 15 alkyl compounds at the example of $\text{EH}_2(t\text{-C}_4\text{H}_9)$ (element $\text{E} = \text{N-Bi}$) were investigated and compared to the group 13 example of $\text{GaH}_2(t\text{-C}_4\text{H}_9)$. With the aid of extensive density functional theory based analysis of atomic and electronic structures at the transition state, we can derive three distinct reaction classes. The gallium compound follows the well-known β -hydride route with participation of an empty p orbital at the metal in a concerted, synchronous fashion, exhibiting a low barrier. For compounds with group 15 elements, we find highly nonsynchronous reactions with high reaction barriers. In the case of nitrogen, a proton-like H atom is transferred via attack of the nitrogen nonbonding electron pair. For the heavier homologues (P-Bi), E-C_α bond breaking occurs first and the H atom does not carry charge at the transition state. The reaction barrier in group 15 homologues is thus determined by the E-C_α bond strength down the group. The results enable a rationale for ligand design for precursors involved in chemical vapor-phase deposition processes because a good ligand needs to stabilize the positive charge at C_α .

■ INTRODUCTION

The understanding of reaction mechanisms for the formation and decomposition of inorganic compounds is of vital importance for progress in many research fields in material sciences. An excellent example is gas-phase chemistry, which can be crucial, e.g., for the conduction of chemical vapor deposition (CVD) techniques like organometallic vapor-phase epitaxy. Here, a clean and well-defined decomposition of the precursor molecules is essential for defect-free thin films.^{1–3} Specifically, the growth of compound semiconductors of groups 13 and 15 (also known as III/V materials) is relevant for optoelectronic device applications.^{4,5} In the current development toward the growth of metastable materials,⁶ lower deposition temperatures are desired. This was not possible with precursor molecules of the first generation that carry hydrogen or methyl substituents because they exhibit large reaction barriers for bond breaking.⁷ The advent of *tert*-butyl-substituted compounds paved the way for improved CVD procedures because of their much lower decomposition temperatures.^{8,9} Typical precursor molecules of this second generation carry larger alkyl ligands like ethyl or *tert*-butyl, e.g., $\text{M}(\text{C}_2\text{H}_5)_3$ ($\text{M} = \text{B-In}$) or $\text{EH}_2(t\text{-C}_4\text{H}_9)$ ($\text{E} = \text{P, As}$). After long-standing discussions in the literature about the relative importance of homolytic dissociation and β -hydrogen elimination channels,^{10–15} the latter was found to be responsible for the low-temperature decomposition characteristics.^{3,9,16–18} In a recent computational study, we have shown that β -hydrogen elimination reactions are indeed the kinetically most favorable gas-phase decomposition pathways under CVD conditions for both group 13 and 15 compounds.¹⁹ Thus, an understanding of

this mechanism is crucial for further advancement in this research field.

β -Hydride elimination of transition-metal^{20,21} and group 13 compounds is well understood and was investigated experimentally^{11,12,22,23} and by quantum-chemical calculations.^{24,25} It can be described as an interaction of the $\sigma(\text{C}_\beta\text{-H}_{\text{tr}})$ bond with the empty p-type orbital at the metal center (see Figure 1a). Thereby, the $\text{C}_\beta\text{-H}_{\text{tr}}$ bond is activated, a hydridic H atom is transferred, and the products are formed. However, how can we understand the respective mechanism from group 15 sources, which exhibit a filled p orbital at the central atom (Figure 1b)? Here, the interaction sketched for group 13 elements (the same

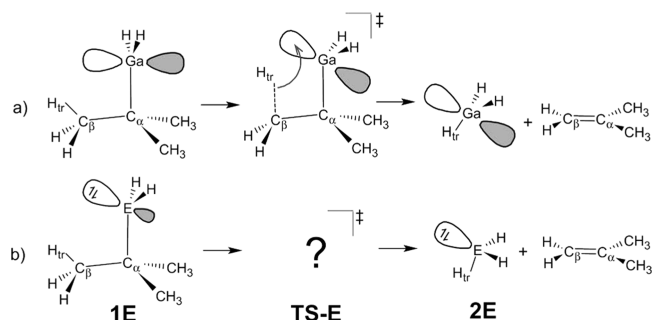


Figure 1. (a) Established mechanism of the β -hydride elimination exemplified for $\text{GaH}_2(t\text{-C}_4\text{H}_9)$. (b) Educt and products of β -hydrogen elimination from mono-*tert*-butylpnictogens ($\text{E} = \text{N-Bi}$) with the unknown TS structure indicated.

Received: March 26, 2015

Published: June 22, 2015

mechanism is found for transition-metal compounds) is not possible because no empty orbital is available to activate the $C_\beta-H_{tr}$ bond. Also, the H_{tr} atom is assumed to not be of hydridic nature; therefore, the usual term to describe this reaction is “ β -hydrogen elimination”.⁹ As an example, the barrier for the reaction of $PH_2(t-C_4H_9)$ were found to be around twice as large as the barrier in $Ga(C_2H_5)_3$, which is already an indication for a different reaction mechanism.¹⁹ It was also suggested in a computational study that β -hydrogen elimination for $AsH_2(t-C_4H_9)$ proceeds in a concerted and more complicated way than the group 13 analogue,²⁴ while early studies at the HF/6-31G level for $PH_2(t-C_4H_9)$ only focused on homolytic dissociation.²⁶

Up to now, there is no conclusive picture of the β -hydrogen elimination reaction in group 15 compounds. It is crucial to have a detailed analysis of this mechanism for an optimization of precursor molecules for decomposition processes but also for a fundamental understanding of the underlying chemistry. Currently, ternary and quaternary compound semiconductors are heavily investigated for new optoelectronic devices, thus creating the need for reliable precursors also for heavier atoms.^{5,27} The inclusion of group 15 elements other than P and As is thus timely and also enables us to discuss trends in the group. In this study, we present a quantum-chemical analysis of the β -hydrogen elimination reaction for $EH_2(t-C_4H_9)$ ($E = N, P, As, Sb, Bi$) in comparison to a group 13 precursor [$GaH_2(t-C_4H_9)$]. Via analysis of the structural and electronic contributions along the path of this intriguing reaction, we shed light on the underlying mechanism. These quantitative analyses are further translated into a model that highlights the differences between β -hydride and β -hydrogen elimination reaction mechanisms and also provides hints toward ligand optimization.

METHODS

Density functional theory with the generalized gradient approximation Perdew–Burke–Ernzerhof (PBE) functional^{28,29} was applied together with the def2-TZVPP³⁰ basis set and effective core potentials for Sb and Bi³¹ for unconstrained optimization of all structures. All subsequent analysis is based on these structures. It was shown that this computational level provides good accuracy in comparison to CCSD(T) benchmark values.¹⁹ The nature of stationary points was confirmed via computation of the Hessian, also enabling the derivation of thermodynamic contributions to reaction energies and barriers ($p = 1$ and 0.05 atm; $T = 298$ and 675 K). The transition state (TS) structures, which connect reactant and product states via a single imaginary vibrational mode, were confirmed by intrinsic reaction coordinate (IRC) calculations. Partial charges were derived via atoms in molecules (AIM)³² as well as natural population analysis (NPA).^{33–35} The topological AIM³⁶ analysis was performed with AIMExt,³⁷ next to Wiberg bond indices (WBI)^{38–40} on the basis of natural atomic orbitals (NAOs)^{33–35} as implemented in Gaussian09.⁴¹ Energy decomposition analysis with natural orbitals for chemical valence (EDA-NOCV)⁴² calculations were performed with ADF⁴³ applying the BP86 functional^{44,45} and the TZ2P+ Slater-type basis set⁴⁶ including scalar relativistic corrections⁴⁷ and frozen core approximation. Molecular orbital (MO) analysis was carried out with this method. EDA-NOCV analysis^{48,49} allows the decomposition of bond energy into electrostatic, Pauli repulsion, and orbital relaxation contributions, subsequent to a structural fragment preparation energy:

$$\Delta E_{\text{bond}} = \Delta E_{\text{prep}} + \Delta E_{\text{elstat}} + \Delta E_{\text{Pauli}} + \Delta E_{\text{orb}} \quad (1)$$

This provides valuable insight into the nature of interactions between two fragments. With the NOCV extension, the orbital relaxation step in the procedure can be quantified by pairs of NOCVs

and interpreted by their respective deformation density contributions $\Delta\rho$. This allows the determination of localized interactions stemming from fragment orbitals together with a quantification of their donating/accepting character by the NOCV eigenvalues $\pm\nu$.⁴² The isosurface value for plotting densities was adjusted to emphasize the nature of MOs and NOCVs.

Analysis of the reaction force $F(\zeta)$ and reaction force constant $\kappa(\zeta)$ ^{50,51} was carried out by numerical differentiation (centered finite differences) from high-resolution IRC calculations along a reaction coordinate ζ with

$$F(\zeta) = -\partial E / \partial \zeta \quad (2)$$

and

$$\kappa(\zeta) = \partial^2 E / \partial^2 \zeta \quad (3)$$

Points of inflection along the IRC can be observed as extrema of $F(\zeta)$, where $\kappa(\zeta) = 0$. Those points separate the IRC into reactant, transition, and product regions. The synchronicity of a reaction can already be evaluated by the symmetry of those regions with respect to the TS.

RESULTS

Structures and Energies. The electronic (ΔE) and Gibbs (ΔG) reaction energies for the β -hydrogen elimination reaction (Figure 1) of mono-*tert*-butyl compounds $EH_2(t-C_4H_9)$ ($E = N-Bi, Ga$) are shown in Table 1. All reactions are endothermic

Table 1. Electronic Reaction Energies ΔE , Gibbs Energies ΔG , Reaction Barriers ΔE^\ddagger and ΔG^\ddagger in kJ mol^{-1} , and Imaginary Modes ν_{imag} in cm^{-1} of the Reactions Introduced in Figure 1 at PBE/def2-TZVPP

| E | ΔE | ΔG | | ΔE^\ddagger | ΔG^\ddagger | | ν_{imag} |
|----|------------|------------|----------|---------------------|---------------------|----------|---------------------|
| | | <i>a</i> | <i>b</i> | | <i>a</i> | <i>b</i> | |
| N | 58.8 | −1.2 | −81.5 | 275.8 | 253.4 | 249.5 | 1402.3 |
| P | 82.6 | 17.0 | −63.1 | 238.8 | 218.0 | 213.2 | 606.3 |
| As | 80.7 | 15.1 | −64.3 | 213.2 | 193.9 | 188.8 | 435.7 |
| Sb | 80.9 | 14.9 | −71.3 | 187.2 | 168.8 | 166.4 | 295.0 |
| Bi | 81.4 | 14.9 | −70.8 | 171.2 | 152.6 | 150.0 | 253.1 |
| Ga | 87.3 | 26.0 | −49.0 | 120.1 | 115.1 | 122.3 | 810.8 |

^a $T = 298$ K and $p = 1$ atm. ^b $T = 675$ K and $p = 0.05$ atm.

or very slightly exothermic at room temperature ($E = N$). It already turns out that three groups of elements can be distinguished: Energies within the group $E = P-Bi$ (**1E** with $E = P-Bi$) are similar to each other, and $E = Ga$ (**1Ga**) has the most positive and $E = N$ (**1N**) the least positive reaction energy (even a negative ΔG value). Note that in CVD processes higher temperatures and lower total pressures are used.^{52,53} Thus, these reactions will become thermodynamically more favorable under deposition conditions, as shown by Gibbs energies for typical conditions of $T = 675$ K and $p = 0.05$ atm in Table 1.¹⁹ The reaction barriers almost linearly decrease within group 15 ($\Delta E^\ddagger = 275.8-171.2$ kJ mol^{-1}), while the barrier for **1Ga** is significantly lower ($\Delta E^\ddagger = 120.1$ kJ mol^{-1}). This generalizes previous findings for **1P**.¹⁹

The vibrational frequencies ν_{imag} of the imaginary modes of the TS structure are highest for $E = N$ (**TS-N**) with 1402.3 cm^{-1} and decrease from 606.3 to 253.1 cm^{-1} for **TS-P** to **TS-Bi**. Notably, $\nu_{\text{imag}}(\text{TS-N})$ is more than twice as large and $\nu_{\text{imag}}(\text{TS-Ga})$ only 204.5 cm^{-1} larger than $\nu_{\text{imag}}(\text{TS-P})$, although the atomic mass of Ga is 5.00 times larger than that of N and 2.25 times larger than that of P. This is a first indication that the imaginary modes of **TS-E** ($E = P-Bi$) are

constituted by an increasing contribution of molecular distortion including the heavy atom E, while TS-N and TS-Ga are dominated by the C_β -H_{tr} stretch mode.

The TS structures for the β -hydrogen elimination reaction for $\text{EH}_2(t\text{-C}_4\text{H}_9)$ (E = N–Bi, Ga) are shown in Figure 2

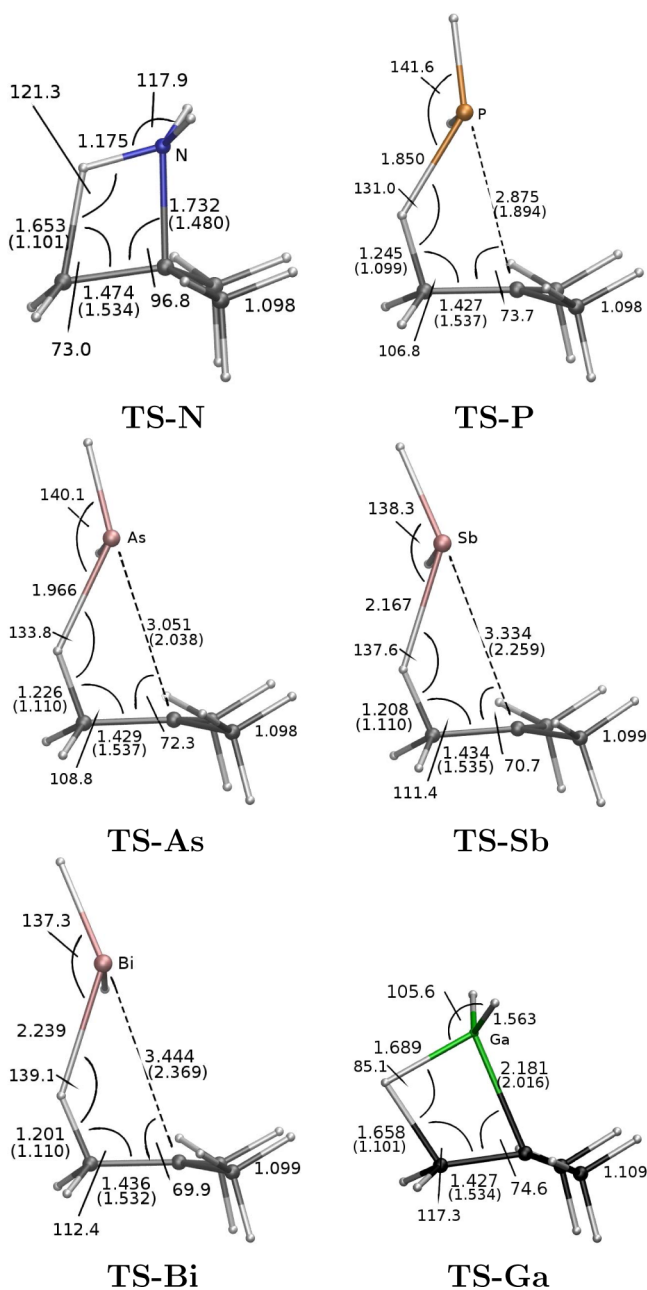


Figure 2. TS structures of $\text{EH}_2(t\text{-C}_4\text{H}_9)$ for β -H elimination reactions with selected bond lengths (in Å) and angles (in degree) for E = N–Bi, Ga. Selected reactant parameters are given in parentheses.

together with selected structural parameters of the reactants. Again, three groups can be distinguished: TS-N, TS-E (E = P–Bi), and TS-Ga. The most pronounced difference is the C_α –E distance, which is reactant-like for TS-Ga, slightly elongated for TS-N, and already considerably lengthened by >1 Å in TS-E (E = P–Bi). Additionally, TS-Ga exhibits a nearly tetrahedral arrangement at the Ga atom, while the ligand arrangement for the N atom in TS-N is closer to trigonal-planar. Another feature is the shape of the four-membered ring as indicated by

the $E\text{--}C_\alpha\text{--}C_\beta$ angle. For TS-Ga and TS-N, the ring structure is distinct, while TS-E (E = P–Bi), on the other hand, show a very distorted ring structure. A further interesting measure is the $C_\beta\text{--}H_{tr}$ bond distance, which is very long for TS-N (1.653 Å) and TS-Ga (1.658 Å), while being close to the bond lengths in the reactants for TS-E (E = P–Bi), with decreasing bond lengths toward the heavier central atoms (1.245 Å for TS-P and 1.201 Å for TS-Bi). For all structures, the $C_\alpha\text{--}C_\beta$ distance shortens by 70–110 pm, leading to values midway between a typical C–C single and a C=C double bond. The EH_2 group in TS-E (E = P–Bi) exhibits a rotation of approximately 30° away from the alkyl ligand, which is later shown to be connected to the formation of nonbonding electron pairs at E.

Analysis along the Reaction Coordinate. The reactant, TS (shaded area), and product regions were identified for the β -H elimination reactions of 1E (E = N, P, Ga) by analysis of the reaction coordinate and are indicated in Figure 3. For 1As–1Bi, features similar to those of 1P were found. The TS region is marked by the two extrema in the force (magenta curves) where most of the bond rearrangements take place.

All molecules investigated undergo concerted elimination mechanisms, as proven by one minimum in the reaction force constant curve (blue curves). This is in line with the vibrational analysis exhibiting one imaginary mode. However, analysis reveals multiple steps during the reactions, indicating a nonsynchronous behavior of bond making and bond breaking.⁵¹ In particular for 1N and 1P, asymmetric shapes of $E(\zeta)$ (black curves) and $F(\zeta)$ (magenta curves) can be observed, which is an indication of nonsynchronicity. The minimum of the force constant $\kappa(\zeta)$ (blue curves) does not coincide with the TS position, which has the same cause. For TS-N (Figure 3, left), we observe a slow energy increase in the first part of the reaction together with small forces because the rotations of the NH_2 and $C_\beta\text{H}_3$ groups taking place there do not require much energy. Then, a sharp increase of the energy curve, a maximum of the force curve, and a deep minimum of $\kappa(\zeta)$ mark breaking of the $C_\beta\text{--}H_{tr}$ bond, which is much more energy-intensive. After the TS, the energy decreases rather slowly with small forces, indicative of bond rearrangements that do not require much energy but take a number of steps, in this case mainly the final breaking of the N– C_α bond.

In the energy curve for TS-P, on the other hand, a steady increase before the TS is observed that can be traced back to the energy-intensive elongation of the P– C_α bond. This is not compensated for by a new bond forming simultaneously. The TS region is very broad here and also includes rotation of the PH_2 group. After the TS, a rapid energy decrease is associated with breaking of the $C_\beta\text{--}H_{tr}$ bond, which is compensated for by formation of the P– H_{tr} bond at the same time.

For TS-Ga, the curves and the TS region appear much more symmetric, indicative of a higher synchronicity of bond making/bond breaking events. The extrema in the reaction force curve have similar heights, which underlines that processes before and after the TS have similar energetic measures. Here, it transpires that, in the case of the group 13 element, bond breaking and bond making occur at similar regions of the reaction coordinate. Thus, an energetic balancing is possible in contrast to the group 15 elements, where bond formation and bond cleavage are more separated events along the reaction coordinate. The structures at the points marking the TS regions are given in the Supporting Information (SI).

Bonding Analysis. Following the discussion of the structural features, we will now shed light on the bonding

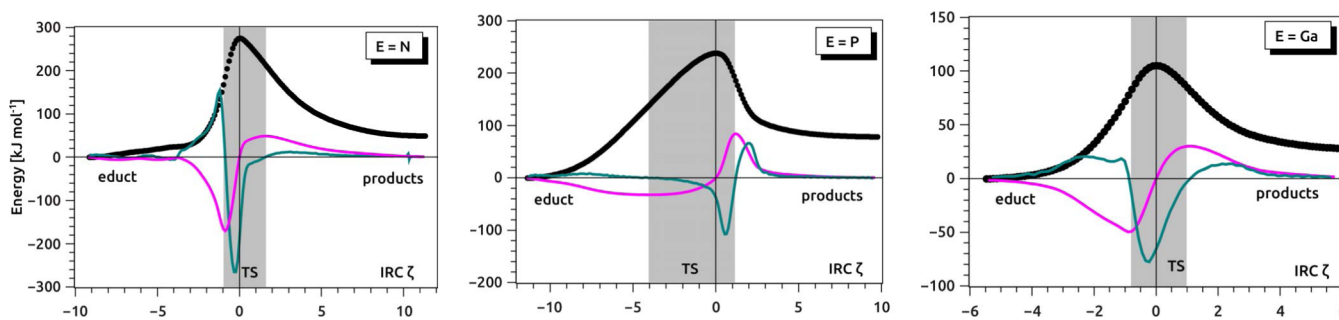


Figure 3. Energy $E(\zeta)$ along an IRC with ζ steps (black dots), reaction force $F(\zeta)$ (magenta curve), and reaction force constant $\kappa(\zeta)$ (blue curve) of the β -H elimination reactions of $\text{EH}_2(t\text{-C}_4\text{H}_9)$ with $\text{E} = \text{N}$ (left), P (center), and Ga (right). The position of the TSs are set to $\zeta = 0$, and the transition regions are separated from the reactant (educt) and product regions by shaded areas as determined by extrema of the reaction force $F(\zeta)$, where $\kappa(\zeta) = 0$.

situation along the reaction path with complementary analysis methods. MO and partial charge analyses are followed by topological analysis of the electron density (AIM) and WBIs before we conclude with an energy decomposition analysis (EDA-NOCV). The combination of these methods leads to a conclusive picture of the reaction mechanism. It should be noted that bonding analysis at the TS is rarely conducted and leads to great insights if an informed choice of methods is applied.⁵⁴

MOs. Selected MOs for TS-N, TS-P, and TS-Ga are shown in Figure 4. Again, TS-P represents the series of heavier group 15 homologues. The character of the highest occupied molecular orbital (HOMO) of TS-N is determined by the overlap of atomic orbitals (AOs) at C_β and H_{tr} with $\sigma(\text{C}_\beta\text{--H}_{\text{tr}})$ -bonding character and the $\text{p}(\text{N})$ orbital, which has lone-pair (LP) character. In the HOMO-2, the second $\text{p}(\text{N})$ orbital with LP character is dominant and an overlap to the $\sigma(\text{C}_\beta\text{--C}_\alpha)$ bond can be identified. The HOMO-3 has N- C_α -bonding character. Both the HOMO and HOMO-1 of TS-P have LP character at P with only minor contributions from the alkyl ligand [$\text{p}(\text{C}_\alpha)$ in the HOMO and $\sigma(\text{C}_\beta\text{--H}_{\text{tr}})$ in HOMO-1]. Only in the HOMO-7 are major contributions from the AOs of C_β and H_{tr} found. For TS-Ga, the HOMO exhibits contributions from $s(\text{H}_{\text{tr}})$ and $\text{p}(\text{C}_\alpha)$, while the HOMO-2 stems from the AOs $\text{p}(\text{C}_\beta)$ and $s(\text{H}_{\text{tr}})$. Information about the nature of the TS can be found here. For TS-N, we find MOs with bonding contributions between all atoms constituting the ring structure. A transformation of the $\sigma(\text{C}_\beta\text{--H}_{\text{tr}})$ and $\sigma(\text{N--C}_\alpha)$ bonds to a $\pi(\text{C}_\beta\text{--C}_\alpha)$ bond can be sketched. Furthermore, an orbital with bonding character between H_{tr} and E was found in TS-N (HOMO-2) and TS-Ga (HOMO), but not among the MOs of TS-E ($\text{E} = \text{P--Bi}$). Orbital overlap between H_{tr} and C_β can be found in the HOMO-2 for TS-Ga and the HOMO-1 of TS-P. Furthermore, a partially empty $s(\text{H}_{\text{tr}})$ orbital is available in TS-N (LUMO+1) and TS-P (LUMO), which is not the case in TS-Ga, where it is fully occupied (contributions in HOMO and HOMO-2) in line with the interpretation of hydridic character. The $s(\text{H}_{\text{tr}})$ orbital can thus serve as a transit orbital for electron density flowing from the LP(E) toward the developing $\pi(\text{C}_\beta\text{--C}_\alpha)$ bond during the reaction. TS-N exhibits one MO with LP character (HOMO-2) at N, while TS-P exhibits two (HOMO and HOMO-1). The latter can be connected to the out-of-plane rotation of the EH_2 group found in the discussion of the TS structures above. While MO analysis thus gives qualitative insight, more quantitative measures are needed for a full description.

Partial Charges. Partial charge analysis gives information about the charge rearrangement in the course of the reaction. In Table 2, we present the absolute partial charges q for important fragments (H_{tr} , EH_2 , and C_4H_8) as well as charge shifts Δq during the elimination reaction. The latter values are given for the steps reactant \rightarrow TS and TS \rightarrow products. The natural-orbital-based NPA charges were chosen, but similar trends are obtained by the electron-density-based AIM scheme (see the SI, Table S1).

First, we look at the charge shifts in the step from reactants to the TS (third column). We see that the β -hydrogen atom H_{tr} gets positively charged by +0.43 e for 1N, while it receives a significant amount of negative charge for 1Ga (−0.27 e). For 1E ($\text{E} = \text{P--Bi}$), H_{tr} remains essentially neutral. A look at the other fragments shows that for 1N the charge is shifted from H_{tr} to the C_4H_8 fragment (−0.46 e), while for 1Ga, the same fragment donates the charge (+0.25 e) to H_{tr} . Thus, we have the picture of a hydridic H atom for 1Ga, while it seems more proton-like for 1N. For 1E ($\text{E} = \text{P--Bi}$), the charge shift as indicated by NPA is found to flow from the C_4H_8 fragment to the EH_2 fragment with less charge shifted for the heavier homologues (−0.52 e for 1P to −0.33 e for 1Bi). This leads to the EH_2 fragment being partially negatively charged at the TS and can be understood as an heterolytic cleavage of the E--C_α bond in 1E ($\text{E} = \text{P--Bi}$) toward the TS. This is also found in the MO analysis, resulting in two MOs with LP character at E (see above).

The charge shift from the TS to the product is also found in Table 2 (fifth column). For 1N, only small values are found in this step, and mainly the surplus charge at the C_4H_8 fragment (−0.13 e) is shifted toward the resulting product 2N. This is in line with analysis of the reaction path and the finding that the majority of rearrangements is found from 1N to TS-N. Similar conclusions can be drawn for 1Ga. For 1E ($\text{E} = \text{P--Bi}$), the charge is shifted from EH_2 to H_{tr} and somewhat less to C_4H_8 . Note that the GaH_2 fragment remains positively charged throughout the reaction, while the NH_2 fragment stays negatively charged. This is in accordance with the electronegativities of the atoms. Because these are the main determining factors for the observed partial charges, the interpretation of charge shifts can be limited, especially for H atoms.^{55,56} We therefore decided to employ further methods to underline our arguments.

AIM and WBIs. The AIM method enables a topological analysis of the electron density and is thus independent of the choice of orbitals. Analysis of the bond paths and bond (or ring) critical points (BCPs and RCPs) helps to identify the

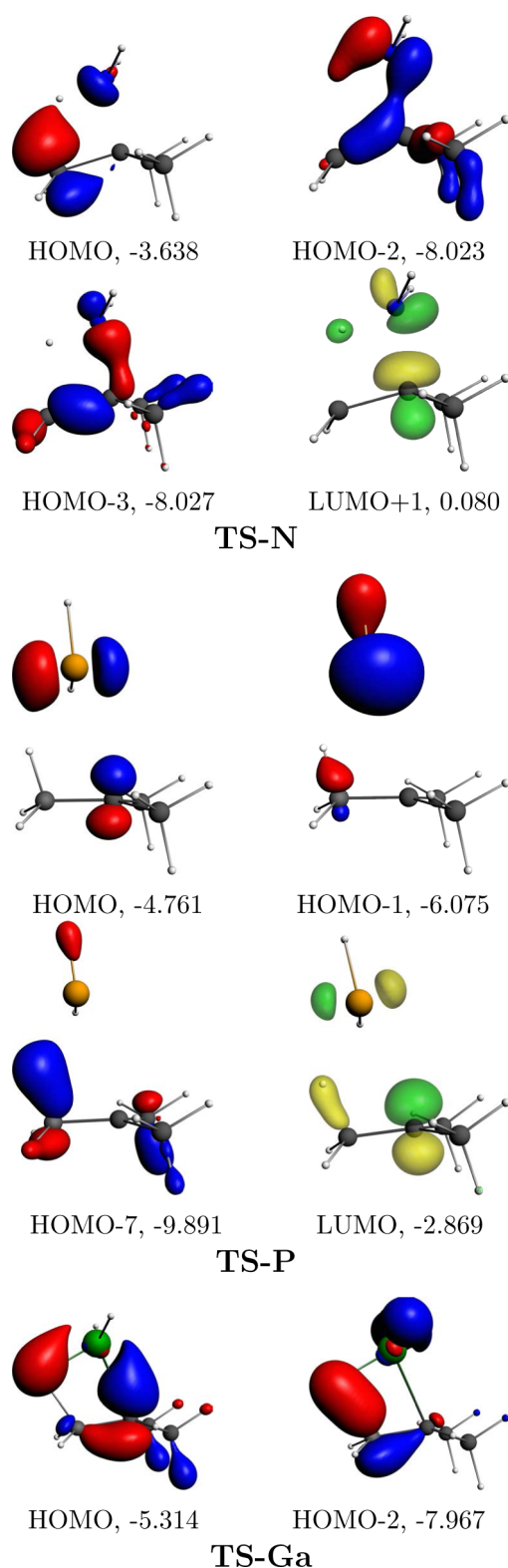


Figure 4. Selected MOs for TS-N (top), TS-P (center), and TS-Ga (bottom) with orbital eigenvalues in electronvolts.

character of an interatomic interaction (Table 3).³⁶ Moreover, the second derivative (Laplacian, $\nabla^2\rho$) of the electron density indicates areas of charge accumulation and depletion. Nevertheless, a bond path should not be taken as proof for a chemical bond.^{57,58} We combine the AIM with a second measure for the breaking and forming of bonds during the elimination

Table 2. NPA Partial Charges q for the Fragments H_{tr} , EH_2 , and C_4H_8 at the Educt State, TS, and Product (prd.) State and Charge Shifts (Δq_{frag}) for $1E \rightarrow TS-E$ and $TS-E \rightarrow 2E + C_4H_8$

| H_{tr} | $q(\text{reactant})$ | Δq_{frag} | | Δq_{frag} | |
|----------|----------------------|-------------------|----------------|-------------------|------------------|
| | | \rightarrow | $q(\text{TS})$ | \rightarrow | $q(\text{prd.})$ |
| N | −0.01 | +0.43 | 0.41 | −0.08 | 0.33 |
| P | 0.00 | +0.08 | 0.09 | −0.55 | −0.46 |
| As | 0.00 | +0.07 | 0.07 | −0.33 | −0.27 |
| Sb | 0.00 | +0.03 | 0.02 | −0.33 | −0.30 |
| Bi | −0.01 | +0.02 | 0.01 | −0.28 | −0.27 |
| Ga | −0.01 | −0.27 | −0.28 | −0.12 | −0.40 |

| EH_2 | $q(\text{reactant})$ | Δq_{frag} | | Δq_{frag} | |
|--------|----------------------|-------------------|----------------|-------------------|------------------|
| | | \rightarrow | $q(\text{TS})$ | \rightarrow | $q(\text{prd.})$ |
| N | −0.32 | +0.04 | −0.28 | −0.05 | −0.33 |
| P | 0.31 | −0.52 | −0.21 | +0.67 | 0.46 |
| As | 0.20 | −0.38 | −0.18 | +0.45 | 0.27 |
| Sb | 0.25 | −0.39 | −0.14 | +0.44 | 0.30 |
| Bi | 0.21 | −0.33 | −0.12 | +0.39 | 0.27 |
| Ga | 0.38 | +0.02 | 0.41 | −0.01 | 0.40 |

| C_4H_8 | $q(\text{reactant})$ | Δq_{frag} | | Δq_{frag} | |
|----------|----------------------|-------------------|----------------|-------------------|------------------|
| | | \rightarrow | $q(\text{TS})$ | \rightarrow | $q(\text{prd.})$ |
| N | 0.33 | −0.46 | −0.13 | +0.13 | 0 |
| P | −0.31 | +0.43 | 0.12 | −0.12 | 0 |
| As | −0.20 | +0.31 | 0.12 | −0.12 | 0 |
| Sb | −0.24 | +0.36 | 0.12 | −0.12 | 0 |
| Bi | −0.20 | +0.31 | 0.11 | −0.11 | 0 |
| Ga | −0.37 | +0.25 | −0.13 | +0.13 | 0 |

reactions. WBIs based on NAOs were calculated for the TS structures, giving an estimate of the number of electrons that populate bonding orbitals.

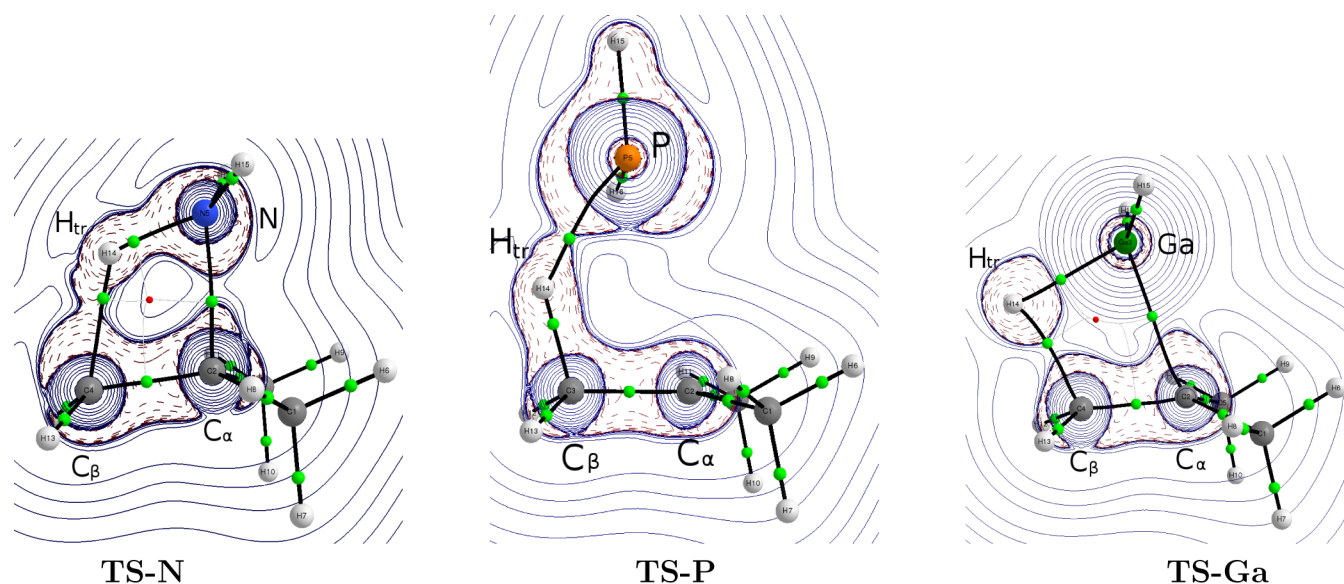
The molecular graph for TS-N in Figure 5 shows a RCP, which necessitates BCPs between all atoms in the ring. The N atom shows an accumulation of charge toward the C_α atom, in line with the bond lengths and the MO picture of the still significant bonding interactions between the two atoms. This is reflected in a considerable density at the BCP (0.12 au) and the largest WBI in the series (0.61). The C_β – H_{tr} bond is already weak here (WBI: 0.30) and strongly polarized toward the C_β atom (BCP lying very close to H_{tr}). The H_{tr} –N bond exhibits already significant values for the density at the BCP (0.20 au) and the WBI (0.48) midway between the reactant and product. Again, the bond is strongly polarized toward the N atom. The C_β – C_α bond exhibits values still closer to a single bond (WBI: 1.23).

The heavier homologues TS-E ($E = P$ –Bi; TS-P is shown in Figure 5) exhibit significant differences. While the change of the C_β – C_α bond order is similar to that of TS-N, the C_β – H_{tr} bond is still much stronger (WBI: 0.57–0.80) but again polarized toward the C atom. The results for the H_{tr} –E and C_α –E bonds differ for AIM and WBI analysis. While the WBIs indicate slightly lower order for the former bond in comparison to TS-N and a significant C_α –E bond order, the AIM results indicate a low density at the BCPs for H_{tr} –E, and for C_α –E, no bond paths are found. Regarding the dependence of the WBIs on orbital partitioning and the erratic trend for TS-Sb and TS-Bi, we prefer to discuss the AIM results in this case. Thus, a negligible C_α –E interaction is found in accordance with the large bond lengths. The contour plot shows electron

Table 3. Electron Densities at BCPs ($\rho[\text{BCP}]$, in au) Together with WBIs for the Four Bonds in the Ring of the TS Structures (Figure 5)

| bond analysis | | reactant ^a | TS-N | TS-P | TS-As | TS-Sb | TS-Bi | TS-Ga | product ^a |
|--|--------------------|-----------------------|------|------|-------|-------|-------|-------|----------------------|
| $\text{C}_\alpha\text{--E}$ | $\rho[\text{BCP}]$ | | 0.12 | | | | | 0.07 | |
| | WBI | 1 | 0.61 | 0.52 | 0.53 | 0.43 | 0.57 | 0.44 | 0 |
| $\text{C}_\beta\text{--H}_{\text{tr}}$ | $\rho[\text{BCP}]$ | | 0.09 | 0.18 | 0.19 | 0.20 | 0.20 | 0.08 | |
| | WBI | 1 | 0.30 | 0.57 | 0.61 | 0.80 | 0.78 | 0.38 | 0 |
| $\text{H}_{\text{tr}}\text{--E}$ | $\rho[\text{BCP}]$ | | 0.20 | 0.07 | 0.06 | 0.05 | 0.04 | 0.08 | |
| | WBI | 0 | 0.48 | 0.37 | 0.34 | 0.15 | 0.50 | 0.47 | 1 |
| $\text{C}_\beta\text{--C}_\alpha$ | $\rho[\text{BCP}]$ | | 0.27 | 0.29 | 0.29 | 0.29 | 0.28 | 0.29 | |
| | WBI | 1 | 1.23 | 1.30 | 1.29 | 1.14 | 1.08 | 1.31 | 2 |

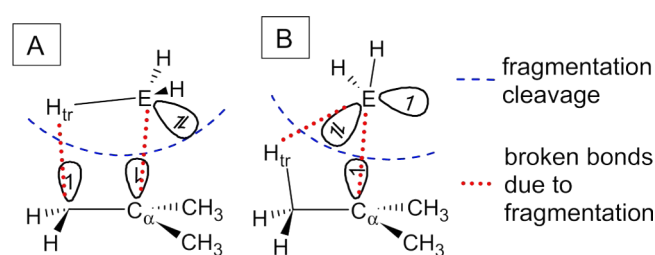
^aIdeal reactant and product WBIs are given to discuss trends. Calculated reactant and product WBIs are provided in the SI.

**Figure 5.** Contour plot of $\nabla^2\rho$ within the $\text{H}_{\text{tr}}\text{--C}_\beta\text{--C}_\alpha\text{--E}$ plane for TS-E ($\text{E} = \text{N}, \text{P}, \text{Ga}$) with BCPs and bond paths from AIM analyses. Dashed red lines indicate areas of electron accumulation (positive $\nabla^2\rho$). Filled blue lines indicate areas of density depletion (negative $\nabla^2\rho$). BCPs are marked by green dots and RCPs by red dots.

accumulation at the P atom, which is in line with the two MOs found exhibiting LP character.

The representative of group 13, TS-Ga, shows RCPs and BCPs similar to those of TS-N; however, significant quantitative differences can be observed. No electron accumulation is found around the Ga atom, in accordance with the absence of a nonbonding electron pair. The $\text{C}_\alpha\text{--Ga}$, $\text{H}_{\text{tr}}\text{--Ga}$, and $\text{C}_\beta\text{--H}_{\text{tr}}$ bonds are less polarized and leave much more density at the H_{tr} atom, again underlining the hydridic character.

Energy Decomposition Analysis. Previous analyses gave insight into charge rearrangement and electron distribution. What is missing as the last piece of the puzzle is analysis of the energetic consequences of this charge flow at the TS. This can be achieved by applying the EDA-NOCV method.⁵⁴ The critical step in every decomposition method is the choice of fragments. The main criterion is a low value for the orbital interaction term (ΔE_{orb}), meaning that the fragments' electronic structures are close to the one in the final molecule.⁵⁹ We tested various schemes and concluded that the fragmentations shown in Figure 6 should be used. The corresponding EDA results are found in the SI (Tables S3–S5). Note that, for $\text{E} = \text{P--Bi}$, fragmentation B with charged (EH_2^+ and C_4H_9^+) or neutral (EH_2^\bullet and $\text{C}_2\text{H}_9^\bullet$) fragments leads to very similar results. These fragmentations indicate

**Figure 6.** Schemes for EDA-NOCV analysis of TS-E separating into (a) EH_3 and C_4H_8 ($\text{E} = \text{Ga}, \text{N}$) or (b) EH_2^\bullet and $\text{C}_2\text{H}_9^\bullet$ ($\text{E} = \text{P--Bi}$) fragments.

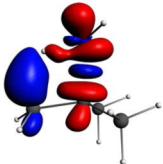
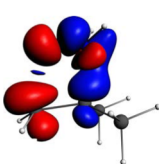
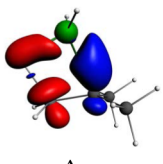
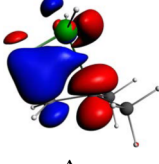
heterolytic and homolytic cleavage of the E--C_α bond, respectively. While the charged fragments are in line with the interpretation of an already broken E--C_α bond (see above), neutral decomposition leads to smaller orbital energy values and is thus presented subsequently.

While analysis of the EDA results can lead to great insight in many occasions,⁶⁰ here we will focus on partitioning of the orbital interaction term ΔE_{orb} in NOCV components. It should, nevertheless, be noted that the same grouping as that observed in the previous sections results from EDA: TS-N and TS-Ga show similar results, and TS-E ($\text{E} = \text{P--Bi}$) represent a separate group with only mild quantitative differences toward heavier

homologues. The discussion will focus on the comparison of compounds analyzed with the same fragmentation to avoid ambiguities.

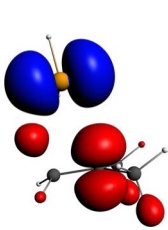
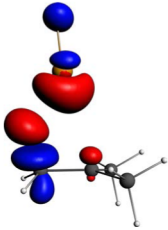
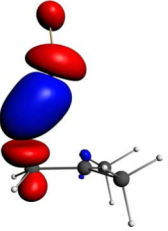
The results of EDA-NOCV analysis are given in Table 4 for fragmentation A (TS-N and TS-Ga) and in Table 5 for

Table 4. Most Significant NOCV Deformation Densities ($\Delta\rho$), Eigenvalues for NOCV Orbitals (ν), and Corresponding Energies (ΔE in kJ mol^{-1}) for TS-N (Top) and TS-Ga (Bottom)^a

| | | | | |
|-------|---|----------------|---|-------------|
| TS-N |  | |  | |
| | $\Delta\rho_1$ | $\Delta\rho_2$ | | |
| | ΔE_1 | ν_1 | ΔE_2 | ν_2 |
| | -497.8 | ± 0.586 | -43.9 | ± 0.151 |
| TS-Ga |  | |  | |
| | $\Delta\rho_1$ | $\Delta\rho_2$ | | |
| | ΔE_1 | ν_1 | ΔE_2 | ν_2 |
| | -369.8 | ± 0.544 | -68.5 | ± 0.198 |

^aThe fragmentation is shown in Figure 6. Charge flow is from red to blue areas.

Table 5. Most Significant NOCV Deformation Densities ($\Delta\rho$), Eigenvalues for NOCV Orbitals (ν), and Corresponding Energies (ΔE in kJ mol^{-1}) for TS-E (E = P–Bi)^a

| | | | | | | |
|-------|---|-------------------------------|---|------------------------|---|------------------------|
| |  | |  | |  | |
| | $\Delta\rho_1^{\beta-\alpha}$ | $\Delta\rho_2^{\alpha+\beta}$ | $\Delta\rho_3^{\alpha+\beta}$ | | | |
| | ΔE_1 | $\nu_1^{\beta-\alpha}$ | ΔE_2 | $\nu_2^{\alpha+\beta}$ | ΔE_3 | $\nu_3^{\alpha+\beta}$ |
| TS-P | -137.2 | ± 0.173 | -23.3 | ± 0.208 | -26.5 | ± 0.174 |
| TS-As | -111.2 | ± 0.163 | -15.3 | ± 0.169 | -19.0 | ± 0.147 |
| TS-Sb | -81.2 | ± 0.144 | -12.0 | ± 0.146 | -14.3 | ± 0.133 |
| TS-Bi | -68.7 | ± 0.119 | -10.4 | ± 0.129 | -10.7 | ± 0.116 |

^aThe fragmentation is shown in Figure 6. Charge flow is from blue to red areas.

fragmentation B [TS-E (E = P–Bi)]. For all TSs, one major NOCV component is found that enables unambiguous interpretation of the orbital contribution to the bond energy. In the case of TS-N, the first deformation density ($\Delta\rho_1$) delivers by far the largest contribution to the orbital relaxation energy ($-497.8 \text{ kJ mol}^{-1}$) and can be identified as a charge shift from the N atom into the region of the $\text{C}_\beta\text{--H}_{\text{tr}}$ bond combined with density accumulation between N and C_α from both atoms.

The second component ($\Delta\rho_2$) shows reverse electron flow: from the $\text{C}_\beta\text{--H}_{\text{tr}}$ region toward the N atom, together with charge shifted to the C_α atom. This contributes far less to the orbital energy ($-43.9 \text{ kJ mol}^{-1}$).

For TS-Ga (Table 4, bottom), essentially the same components are found but with inverse energy ordering. The first deformation density ($\Delta\rho_1$) shows the charge flow from the C_β and H_{tr} atoms into the Ga--C_α bonding region and delivers a stabilization of $-369.8 \text{ kJ mol}^{-1}$. The second one ($\Delta\rho_2$) now is the inverse charge flow from the C_α and Ga atomic orbitals toward the $\text{C}_\beta\text{--H}_{\text{tr}}$ bond and into the ring structure. This contributes $-68.5 \text{ kJ mol}^{-1}$ to the orbital energy. We can thus quantify the results from the partial charge and MO analysis above and conclude that the charge shift in the TS is reverse for TS-N in comparison to TS-Ga. While N is donating, Ga is accepting electron density at the TS.

The results for TS-E (E = P–Bi) are found in Table 5. Because of the unrestricted fragments, we have α - and β -NOCV components. As is often observed, these spin densities can have either the same charge flow or a reversed one. Here, the first deformation density ($\Delta\rho_1$) shows the latter behavior. Thus, we subtracted the respective energies and eigenvalues as well as the densities. It appears that the net charge flow is from the $p(\text{C}_\alpha)$ and the H_{tr} region to the LP region of E. This delivers stabilization energies of up to $-137.2 \text{ kJ mol}^{-1}$ for TS-P and still $-68.7 \text{ kJ mol}^{-1}$ for TS-Bi. For the other two major deformation densities, both spins exhibit the same charge shift pattern and are thus added up. Some more energy is gained by donation from $\text{LP}(\text{E})$ and H_{tr} to C_β ($\Delta\rho_2$) and into the E--H_{tr} bonding region ($\Delta\rho_3$). The absence of charge donation between C_α and E supports the above analyses in the finding that this bond is already broken. The resulting picture is a slowly evolving E--H_{tr} bond with density mainly stemming from E and a strong charge accumulation at E.

DISCUSSION

We will now discuss the observations from the analysis methods employed and arrive at a comprehensive picture of the β -H elimination mechanisms for the three distinct groups identified above: 1N, 1E (E = P–Bi), and 1Ga.

β -Proton Elimination of 1N. 1N exhibits the largest reaction barrier in the series. Analysis of the reaction path (Figure 3) shows a sharp increase in the reaction force close to the TS connected to this energy increase and a narrow transition region. From the reactant to the TS, the following changes in the chemical bonds can be identified:

(i) Breaking of the $\sigma(\text{C}_\beta\text{--H}_{\text{tr}})$ bond. The increased bond length (1.653 \AA), a low WBI (0.30), and electron density at the BCP ($\rho[\text{BCP}] = 0.09 \text{ au}$) are strong indicators for bond cleavage. The electrons are shifted from the bonding region toward the C_β atom at the TS, which can be seen in the charge shift analysis [$\Delta q(\text{H}_{\text{tr}}) = +0.41 \text{ e}$ and $\Delta q(\text{C}_4\text{H}_8) = -0.46 \text{ e}$] and the HOMO, which has mainly C_β character.

(ii) Formation of the $\sigma(\text{N--H}_{\text{tr}})$ bond. The N--H_{tr} distance (1.175 \AA) is already close to the distance in 2N (1.022 \AA). WBI (0.48) and $\rho[\text{BCP}]$ (0.20 au) exhibit significant values underlined by the HOMO–2 with bonding character between the atoms. The electrons for the bond stem from $\text{LP}(\text{N})$, as can be seen qualitatively in the polar bond of the AIM analysis and quantitatively in the deformation density $\Delta\rho_1$ of EDA-NOCV analysis ($\Delta E_1 = -497.8 \text{ kJ mol}^{-1}$).

Because the $1s(\text{H}_{\text{tr}})$ orbital has contributions to both the $\sigma(\text{C}_\beta\text{--H}_{\text{tr}})$ and $\sigma(\text{H}_{\text{tr}}\text{--N})$ bonds, it can be understood as being

an “electron transit orbital” for the charge flow between these regions. The H_{tr} atom exhibits substantial positive partial charge at the TS ($q = +0.41$ e). It can thus best be interpreted as being proton-like. It appears as if the nonbonding electron pair of the N atom pushes the electron density via the $s(H_{tr})$ orbital toward the C_β atom. Additionally, it is found that the $\sigma(N-C_\alpha)$ bond is only moderately weakened (slight bond elongation, high WBI, and BCP and MOs with bonding character) and the $\pi(C_\beta-C_\alpha)$ bond only starts to form (increased WBI and bond shortening).

After the TS, the reaction force analysis shows a broader transition region with more rearrangements toward the products. The reaction energy is the only exothermic at ambient conditions ($\Delta G = -1.2$ kJ mol⁻¹). The only major change in chemical bonds is as follows:

(i) $\sigma(N-C_\alpha)$ bond breaking. The charge is shifted from C_4H_8 to NH_3 , as indicated by the partial charge analysis. The $\pi(C_\beta-C_\alpha)$ bond constitutes mainly the electron density from the C_α atom.

β -Hydrogen Elimination of 1E (E = P–Bi). The reaction barriers for 1E (E = P–Bi) are between 1N and 1Ga, with values decreasing toward heavier homologues. All reactions are equally endothermic at ambient conditions and only become viable at CVD conditions. The reaction path analysis shows an extended transition region before the TS with rather small forces and a smooth change in the force constant. This can be understood by the only significant bond change from the reactant to TS:

(i) Breaking of the $\sigma(E-C_\alpha)$ bond. The E– C_α bond lengths increase by approximately 1 Å. This is accompanied by rotation of the EH_2 moiety. All electronic indicators (WBI, $\rho[BCP]$, MO, EDA-NOCV) provide evidence for complete cleavage of this bond at the TS. The charge is shifted to the E atom, which can be deduced from the partial charge [$\Delta q(EH_2) = -0.52$ to -0.31 e] and MO analysis [HOMO and HOMO–1 with LP(E) character]. This charge stems from the C_4H_8 fragment, as found by partial charge shifts and EDA-NOCV ($\Delta E_1 = -137.2$ to -68.7 kJ mol⁻¹). The trend observed for the reaction barriers (lower for heavier homologues) can thus be understood from the decreasing E– C_α bond strength from P to Bi, which makes it increasingly easy to cleave the E– C_α bonds.

All other bonds are only mildly changed from the reactant to TS, as can be seen from the bond lengths being close to the reactant and the small changes in the electronic indicators. The interaction between E and H_{tr} is still quite weak; e.g., the bond length for TS-P (1.850 Å) is still much longer than that for 2P (1.431 Å), underlined by electronic analysis (small $\rho[BCP]$ and no bonding MO). H_{tr} is essentially neutral at the TS [$\Delta q(EH_2) = +0.08$ to $+0.02$ e]. Thus, the H atom transferred is best understood to be a neutral H atom.

From the TS to product, the changes indicated by reaction path analysis point toward a quite rapid development to the products: (i) The E– H_{tr} bond formed is initiated by the electrons from LP(E). (ii) The $\pi(C_\beta-C_\alpha)$ bond is formed with electron density from the $\sigma(C_\beta-H_{tr})$ bond. The $1s(H_{tr})$ orbital can act as a transit orbital for the electronic rearrangement because it is partially occupied in the TS.

β -Hydride Elimination of 1Ga. The reaction barrier for 1Ga is the lowest in the series, while the reaction is also the most endothermic one. Reaction path analysis reveals rather symmetric changes before and after the TS (synchronous reaction). The $\sigma(C_\beta-H_{tr})$ bond is strongly elongated ($d = 1.658$ Å) and small WBI (0.38) and $\rho[BCP]$ (0.09 au) are

observed. It is not completely broken, as a bonding MO (HOMO–2) indicates. The charge is shifted from the region of the $\sigma(C_\beta-H_{tr})$ bond toward the Ga and C_α atoms, as shown by EDA-NOCV ($\Delta E_1 = -369.8$ kJ mol⁻¹).

H_{tr} receives a negative partial charge ($\Delta q = -0.27$ e) before the TS, which stems almost entirely from the C_4H_8 fragment ($\Delta q = +0.25$ e). This indicates the transfer of a H_{tr} atom with hydridic character, as commonly assumed. The TS exhibits a tetrahedral arrangement at the Ga atom, enabling the transfer of this hydridic H_{tr} to the GaH_2 fragment.

All other bonds in the system are about to form [$Ga-H_{tr}$ and $\pi(C_\beta-C_\alpha)$] or break ($Ga-C_\alpha$) simultaneously at the TS. The formation of the $Ga-H_{tr}$ bond is completed by electron transfer from the C_4H_8 fragment [$\Delta q(TS \rightarrow \text{product}) = +0.13$ e], and the elimination closes by breaking the $Ga-C_\alpha$ bond. The rearrangements necessary for these two processes are revealed in the reaction path analysis.

CONCLUSION

β -H elimination reactions for group 15 alkyl species differ significantly from the respective group 13 compounds. For the example of $EH_2(t-C_4H_9)$ with E = N–Bi and Ga, we find three distinct mechanisms summarized in Figure 7.

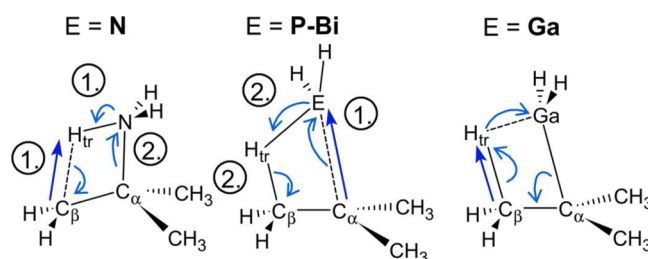


Figure 7. Chronology of the reaction steps for β -H elimination reactions for $EH_2(t-C_4H_9)$ with E = N (left), E = P–Bi (center), and E = Ga (right). Electron shifts (bent arrows) and bond-length elongations (straight arrows) before (1.) and after (2.) the TS are highlighted.

The H atom transferred (H_{tr}) has either protic (E = N), neutral (E = P–Bi), or hydridic (E = Ga) character at the TS. For group 15 elements, we find a nonsynchronous sequence of the reaction steps, while it is synchronous for group 13. Furthermore, the chronologies of the steps during the reaction differ for the three species. For E = N, the $C_\beta-H_{tr}$ bond is elongated in conjunction with electron transfer out of $\sigma(C_\beta-H_{tr})$ toward $\pi(C_\beta-C_\alpha)$. In this process, the LP(N) “attacks” the protic H atom. The charge flow is clockwise in Figure 7. After the TS, the N– C_α bond is broken, and the products are formed.

For E = P–Bi, the barrier is exclusively determined by cleavage of the E– C_α bond along with electron transfer, leading to two LPs at E. All other bond rearrangements occur after the TS.

For E = Ga, the reaction is found to proceed rather symmetrically around the TS. Before the TS, all bonds are stretched, with the majority change in $C_\beta-H_{tr}$. Charge accumulation at the H_{tr} atom renders it hydridic. After the TS, synchronous bond making/bond breaking is observed.

The main reason for the higher barrier of β -H elimination reactions in group 15 compounds is thus the nonsynchronicity of the reaction steps, in contrast to a synchronous bond rearrangement in group 13 alkyls. The filled p orbital at E

requires bond breaking to occur before new bonds are formed. This leads to energetically high-lying TSs. The reason that this reaction can still occur although no acceptor orbital is available lies in the protic character of the transferred H_{tr} atom (E = N) or the possibility of accommodating E–C_α bond breaking before E–H_{tr} bond formation occurs (E = P–Bi). The trend in group 15 is thus determined by the E–C_α bond strengths, which is weaker for the heavier homologues, in line with lower-lying TSs. The last mechanism requires a good ability of the C_α atom to stabilize the positive partial charge occurring in the TS. This knowledge can be used to design new group 15 precursors containing ligands that stabilize this charge at C_α even better than the *tert*-butyl ligand.⁶¹

■ ASSOCIATED CONTENT

■ Supporting Information

Absolute partial charges (NPA and AIM), reactant and product WBI, structures at inflection points along the IRC, EDA results from different fragmentations, Cartesian coordinates, and absolute energies for all species calculated. The Supporting Information is available free of charge on the ACS Publications website at DOI: 10.1021/acs.inorgchem.5b00687.

■ AUTHOR INFORMATION

Corresponding Author

*E-mail: tonner@chemie.uni-marburg.de. Phone: +49 (0) 6421-2825418. Fax: +49 (0) 6421-2821826.

Notes

The authors declare no competing financial interest.

■ ACKNOWLEDGMENTS

We thank the DFG (Research Training Group 1782) for funding and Prof. Jörg Sundermeyer (Marburg) for raising our interest in this issue. A.S. thanks the Beilstein Institut, Frankfurt/Main, Germany, for support. Computational support from HRZ Marburg, LOEWE-CSC Frankfurt, and HLR Stuttgart is acknowledged.

■ REFERENCES

- (1) Brauers, A. *Prog. Cryst. Growth Charact.* **1991**, *22*, 1–18.
- (2) Brauers, A. *J. Cryst. Growth* **1991**, *107*, 281–289.
- (3) Russell, D. K. *Chem. Vap. Deposition* **1996**, *2*, 223–233.
- (4) Liang, D.; Bowers, J. E. *Nat. Photonics* **2010**, *4*, 511–517.
- (5) Liebich, S.; Zimprich, M.; Beyer, A.; Lange, C.; Franzbach, D. J.; Chatterjee, S.; Hossain, N.; Sweeney, S. J.; Volz, K.; Kunert, B.; Stolz, W. *Appl. Phys. Lett.* **2011**, *99*, 071109-1–071109-4.
- (6) Kunert, B.; Volz, K.; Nemeth, I.; Stolz, W. *J. Lumin.* **2006**, *121*, 361–364.
- (7) Manasevit, H. M. *Appl. Phys. Lett.* **1968**, *12*, 156–159.
- (8) Stringfellow, G. B. *J. Electron. Mater.* **1988**, *17*, 327–335.
- (9) Stringfellow, G. B. *Mater. Sci. Eng., B* **2001**, *87*, 97–116.
- (10) Speckman, D. M.; Wendt, J. P. *J. Appl. Phys.* **1991**, *69*, 3316–3323.
- (11) Murrell, A. J.; Wee, A. T. S.; Fairbrother, D. H.; Singh, N. K.; Foord, J. S.; Davies, G. J.; Andrews, D. A. *J. Appl. Phys.* **2013**, *68*, 4053–4063.
- (12) Buchan, I.; Yu, M. L. *Surf. Sci.* **1993**, *280*, 383–392.
- (13) Li, S. H.; Larsen, C. A.; Buchan, N. I.; Stringfellow, G. B. *J. Electron. Mater.* **1989**, *18*, 457–464.
- (14) Paputa, M. C.; Price, S. J. W. *Can. J. Chem.* **1979**, *57*, 3178–3181.
- (15) Lee, P. W.; Omstead, T. R.; McKenna, D. R.; Jensen, K. F. *J. Cryst. Growth* **1987**, *85*, 165–174.
- (16) Bahlawane, N.; Reilmann, F.; Salameh, L.-C.; Kohse-Höinghaus, K. *J. Am. Soc. Mass Spectrom.* **2008**, *19*, 947–954.
- (17) Fan, G.; Hoare, R.; Pemble, M.; Povey, I.; Taylor, A. *J. Cryst. Growth* **1992**, *124*, 49–55.
- (18) Larsen, C. A.; Buchan, N. I.; Li, S. H.; Stringfellow, G. B. *J. Cryst. Growth* **1989**, *94*, 663–672.
- (19) Stegmüller, A.; Rosenow, P.; Tonner, R. *Phys. Chem. Chem. Phys.* **2014**, *16*, 17018–17029.
- (20) Elschenbroich, C.; Salzer, A. *Organometallics: A Concise Introduction*; Wiley-VCH: Weinheim, Germany, 1992; p 198.
- (21) Housecroft, C. E.; Sharpe, A. *Inorganic Chemistry*; Pearson/Prentice Hall: New York, 2005; p 721.
- (22) Lee, J.; Kim, Y.; Anderson, T. *ECS Trans.* **2009**, *25*, 41–49.
- (23) Banse, B. A.; Creighton, J. R. *Surf. Sci.* **1991**, *257*, 221–229.
- (24) Boero, M.; Morikawa, Y.; Terakura, K.; Ozeki, M. *J. Chem. Phys.* **2000**, *112*, 9549–9556.
- (25) Ryan, C.; de Lewis, A. K.; Caddick, S.; Kaltsoyannis, N. *Theor. Chem. Acc.* **2011**, *129*, 303–312.
- (26) Hiraoka, Y. S.; Mashita, M.; Tada, T.; Yoshimura, R. *Appl. Surf. Sci.* **1992**, *60–61*, 246–250.
- (27) Koukourakis, N.; Buckers, C.; Funke, D. A.; Gerhardt, N. C.; Liebich, S.; Chatterjee, S.; Lange, C.; Zimprich, M.; Volz, K.; Stolz, W.; Kunert, B.; Koch, S. W.; Hofmann, M. R. *Appl. Phys. Lett.* **2012**, *100*, 092107-3.
- (28) Perdew, J.; Burke, K.; Ernzerhof, M. *Phys. Rev. Lett.* **1996**, *77*, 3865–3868.
- (29) Perdew, J.; Burke, K.; Ernzerhof, M. *Phys. Rev. Lett.* **1997**, *78*, 1396.
- (30) Weigend, F.; Ahlrichs, R. *Phys. Chem. Chem. Phys.* **2005**, *7*, 3297–3305.
- (31) Metz, B.; Stoll, H.; Dolg, M. *J. Chem. Phys.* **2000**, *113*, 2563–2569.
- (32) Biegler-König, F. W.; Bader, R. F. W.; Tang, T.-h. *J. Comput. Chem.* **1982**, *3*, 317–328.
- (33) Weinhold, F.; Landis, C. A. *Natural Bond Orbital Donor–Acceptor Perspective*; Cambridge University Press: Cambridge, U.K., 2005.
- (34) Reed, A. E.; Weinstock, R. B.; Weinhold, F. *J. Chem. Phys.* **1985**, *83*, 735–746.
- (35) Reed, A. E.; Weinhold, F. *J. Chem. Phys.* **1983**, *78*, 4066–4073.
- (36) Weinhold, R. *Atoms in Molecules—A Quantum Theory*; Oxford University Press: Oxford, U.K., 1990.
- (37) Keith T. A. *AIMExt Professional*; TK Gristmill Software: Overland Park, KS, 2015. aim.tkgristmill.com (accessed June 16, 2015).
- (38) Wiberg, K. *Tetrahedron* **1968**, *24*, 1083–1096.
- (39) Borisova, N.; Semenov, S. *Vestn. Leningr. Univ.* **1973**, *16*, 119.
- (40) de Giambiagi, M.; Grempel, D.; Heyman, C. *J. Chim. Phys.* **1975**, *72*, 15–22.
- (41) Frisch, M. J.; et al. *Gaussian09*, revision C.01; Gaussian Inc.: Wallingford, CT, 2010.
- (42) Mitoraj, M. P.; Michalak, A.; Ziegler, T. *J. Chem. Theory Comput.* **2009**, *5*, 962–975.
- (43) ADF 2010.02; Baerends, F.; et al. *J. Comput. Chem.* **2010**, *22* (9), 931–967.
- (44) Becke, A. *Phys. Rev. A* **1988**, *38*, 3098–3100.
- (45) Perdew, J. *Phys. Rev. B* **1986**, *34*, 8822–8824.
- (46) Chong, D. *J. Comput. Chem.* **2004**, *25*, 1030–1036.
- (47) Lenthe, E. V.; Baerends, E. J.; Snijders, J. G. *J. Chem. Phys.* **1993**, *99*, 4597–4610.
- (48) Ziegler, T.; Rauk, A. *Theor. Chim. Acta* **1977**, *46*, 1–10.
- (49) Kitaura, K.; Morokuma, K. *Int. J. Quantum Chem.* **1976**, *10*, 325–340.
- (50) Politzer, P.; Toro-Labbé, A. *J. Chem. Sci.* **2005**, *117*, 467–472.
- (51) Politzer, P.; Murray, J.; Jaque, P. *J. Mol. Model.* **2013**, *4111*–4118.
- (52) Kunert, B.; Volz, K.; Koch, J.; Stolz, W. *J. Cryst. Growth* **2007**, *298*, 121–125.
- (53) Beyer, A.; Ohlmann, J.; Liebich, S.; Heim, H.; Witte, G.; Stolz, W.; Volz, K. *J. Appl. Phys.* **2012**, *111*, 083534-1–083534-6.
- (54) Hermann, M.; Goedecke, C.; Jones, C.; Frenking, G. *Organometallics* **2013**, *32*, 6666–6673.

- (55) Martin, F.; Zipse, H. *J. Comput. Chem.* **2005**, *26*, 97–105.
- (56) Guerra, C. F. *J. Comput. Chem.* **2004**, *25*, 189–210.
- (57) Bader, R. F. W. *J. Phys. Chem. A* **2009**, *113*, 10391–10396.
- (58) Cerpa, E.; Krapp, A.; Vela, A.; Merino, G. *Chem.—Eur. J.* **2008**, *14*, 10232–10234.
- (59) Tonner, R.; Frenking, G. *Chem.—Eur. J.* **2008**, *14*, 3260–3272.
- (60) Hopffgarten, M. v.; Frenking, G. *WIREs Comput. Mol. Sci.* **2012**, *2*, 43–62.
- (61) Stegmüller, A.; Tonner, R. *Chem. Vap. Deposition* submitted, 2015.